35th Annual International Conference of the IEEE EMBS
Osaka, Japan, 3 - 7 July, 2013

Relationships Between Local Geometrical Features and Hemodynamic Flow Properties

Bernard Chiu, Yimin Chen, Gador Canton and William S. Kerwin

Abstract— **Stroke is among the leading causes of death and disability worldwide. Most strokes are ischemic, mostly caused by the blockage of a cerebral artery by a thrombotic embolus. Carotid atherosclerosis and the subsequent plaque rupture can be a major source of these emboli. It is well known that blood flow affects where atherosclerotic plaque will arise. In particular, vascular wall shear stress (WSS) has been linked to the initiation and progression of carotid plaque. However, it is difficult to measure WSS *in vivo* and it is time-consuming to compute WSS using computational fluid dynamics packages. The goals of this paper are (i) to identify a set of *local* geometric parameters that are correlated with WSS and (ii) to develop a regression model to predict WSS from the geometric parameters. We validated our regression model using the root mean squared error (RMSE), adjusted R^2 and Akaike information criterion (AIC). The experimental study involved six carotid arteries with the internal and external carotid arteries (ICA and ECA respectively) analyzed separately. The adjusted R^2s for 9 of the 12 branches were higher than 0.8. Since the proposed local geometric parameters can be obtained efficiently, these parameters can potentially be used as carotid disease phenotypes that will allow for a much more cost-effective method to identify subjects with elevated stroke risk.**

I. Introduction

Carotid atherosclerosis is a focal disease occurring predominantly at bifurcations [1], [2]. Numerous studies have shown that hemodynamic forces - especially low and oscillatory wall shear stress (WSS) - are linked to the initiation and progression of plaque development [3]. However, current technology for measuring WSS *in vivo* hinges on many assumptions regarding the hemodynamic properties of the blood flow and is not reliable [4]. Numerical techniques in obtaining time-resolved wall shear stress distribution have been developed and are currently available as commercial computational fluid dynamics (CFD) packages [5]–[8]. A major limitation of CFD is that it is computationally intensive and time-consuming. In our experience, it took 15 hours to complete the computation of WSS for three pulse cycles using a commercial CFD package on an Intel Xeon 2.0 GHz CPU with 8.0 GB memory. This limitation precludes the use of CFD in large-scale clinical trials, and therefore, our previous CFD studies involved only a very small population (~ 10) [9].

Recent studies have examined the correlation between the geometry of the bifurcation and hemodynamic parameters, such as WSS and oscillatory shear index (OSI) [10], [11]. The success of these studies suggests the use of geometric parameters to predict flow parameters. However, existing geometric parameters, such as the bifurcation angle, tortuosity and ratio between different branches of the carotid artery [11], [12], are global in nature, while the distribution of hemodynamic parameters are local and computed on a point-by-point basis. Thus, a set of local parameters based on carotid surface geometry needs to be developed that will improve the accuracy of the prediction of flow parameters.

The goal of this paper is to lay the foundation for a model predicting the magnitude of WSS from *local* geometric parameters. Since geometric quantities can be computed efficiently [13], if such a model is established and thoroughly validated, geometric parameters would become surrogate risk markers for cerebrovascular events that can be obtained in a much more cost-effective way than WSS.

II. Methods

A. Carotid MR Imaging and Geometric Model Construction

The MRI acquisition protocol was described in detail in [9]. MR images of five contrast weights were registered and displayed using an in-house image analysis software (CASCADE [14]). The arterial lumen boundary for each axial MR image was segmented on CASCADE. The mesh generation and WSS calculation procedures were described in [9] and are summarized here. For each artery, an unstructured tetrahedal mesh was reconstructed from a stack of 2D segmented contours using a customized version of the MATLAB code developed in [15]. This mesh was imported into a CFD software package (COMSOL Multiphysics, Stockholm, Sweden) in which Navier-Stroke equations were solved. The computation time step was 10ms and three cardiac cycles were simulated. The WSS computed was colour-coded and superimposed on the carotid surface (Fig. 1(b)).

B. Carotid Surface Centerline

The carotid surface was reconstructed from a stack of 2D segmented contours using the method described in [16], which generated a membership function with a value of 1 inside the contours and 0 outside the contours and interpolated this function onto a dense grid. The carotid surface was then extracted from this membership function using the marching cube algorithm [17]. The centerline of the surface

B. Chiu is with Department of Electronic Engineering, City University of Hong Kong, Hong Kong bcychiu@cityu.edu.hk

Y. Chen is a PhD graduate student in Department of Electronic Engineering, City University of Hong Kong, Hong Kong yiminchen3@student.cityu.edu.hk

G. Canton is with Department of Mechanical Engineering, University of Washington, Seattle, Washington, USA gcanton@u.washington.edu

W. S. Kerwin is with Department of Radiology, University of Washington, Seattle, Washington, USA bkerwin@u.washington.edu

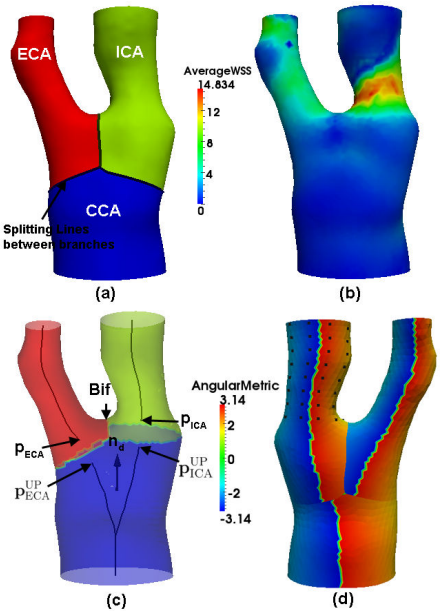

Fig. 1. (a) shows how the ECA, ICA and CCA were decomposed by Antiga's algorithm [18]. (b) shows the time-averaged WSS (in Pa) superimposed on the carotid surface. (c) shows how our proposed algorithm split the carotid artery into three branches. (d) The carotid surface with the circumferential coordinate colour-coded and superimposed.

was generated using the algorithm described in [18], which was implemented as an open-source software known as the Vascular Modeling Toolkit (VMTK) (*www.vmtk.org*).

C. Branch Splitting

WSS distributions on the common, internal and external carotid arteries (CCA, ICA and ECA respectively) are quite different (Fig. 1(b)) and were analyzed separately in this study. Each carotid surface was therefore required to be decomposed into three branches.

Antiga et al. [18] described a branch decomposition algorithm based on four reference points. Two points on each centerline were defined: the first is located where the centerline of one branch intersects another centerline's tube (where a tube is the envelope of the maximum inscribed sphere along a centerline, defined mathematically in Eq. (2) in [18]) and is denoted as C_1^{ECA} and C_1^{ICA} for the two branches. The second is located one maximum inscribed sphere upstream and denoted as C_2^{ECA} and C_2^{ICA} for the two branches (Fig. 2 of [18]). Points on the carotid surface were classified as belonging to the CCA, ICA and ECA according to their distances from these reference points. The problem of this branch splitting procedure is that the decomposed ICA and ECA extends too much to the CCA (Fig. 1(a)). This is an issue because WSS changes abruptly when blood flows from the CCA to ICA or ECA (Fig. 1(b)) and the correlation between geometric parameters and WSS should be studied separately for each branch.

To address this issue, we defined the reference points differently. Before defining the reference points, the location of the bifurcation apex must be defined. This definition depends on two items defined in [18] (a) the splitting line between the three branches and (b) the *UpNormal* component of the reference frame (n_d in Fig. 2 of [18]). The splitting lines between branches decomposed according to [18] are shown in Fig. 1(a). n_d is the unit vector pointing downstream with average direction of $C_1^{\mathrm{ECA}} - C_2^{\mathrm{ECA}}$ and $C_1^{\mathrm{ICA}} - C_2^{\mathrm{ICA}}$. The bifurcation point was defined to be the point that has the maximum dot product with n_d over all points on the splitting line (Fig. 1(c)). Then four reference points were defined: p_{ECA} and p_{ICA} are points on the centerlines of ECA and ICA branches respectively that are closest to the bifurcation. $p_{\mathrm{ECA}}^{\mathrm{UP}}$ is located one maximum inscribed sphere upstream from p_{ECA} and $p_{\mathrm{ICA}}^{\mathrm{UP}}$ was defined similarly (Fig. 1(c)). For the centerline generated for the CCA-ECA branch, the centerline segment distal to p_{ECA} was labeled *ECA Line* and the segmental proximal to $p_{\mathrm{ECA}}^{\mathrm{UP}}$ forms the first part of the *CCA Line*. Similarly, for the centerline generated for the CCA-ICA branch, the centerline segment distal to p_{ICA} was labeled *ICA Line* and the segmental proximal to $p_{\mathrm{ICA}}^{\mathrm{UP}}$ forms the second part of the *CCA Line*. The distances between each point, p, on the carotid surface and the *ICA, ECA and CCA Lines* were computed. Point p belongs to a branch if it is closest to the corresponding line among the three lines. Fig. 1(c) shows the results of the proposed branch decomposition method.

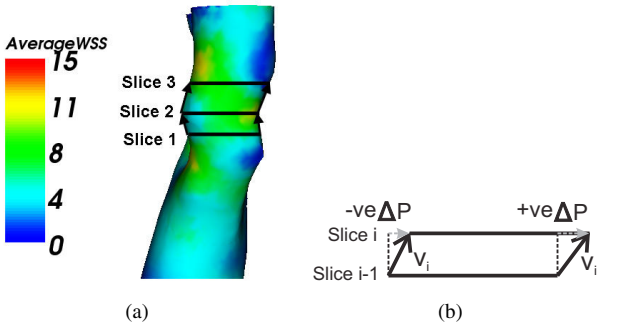

Fig. 2. Definition of a geometric parameter, *Change of Position* (ΔP). (a) A carotid surface with three transverse contours of the ICA displayed. (b) A schematic showing examples of positive and negative ΔP.

D. Extraction of Local Geometric Parameters

Fig. 2(a) shows the ICA of a carotid artery with WSS superimposed. We defined three transverse slices in the figure. Suppose each point on a transverse slice has a correspondence point on the slice immediately distal to it. We denote the vector pointing from a point, p_{i-1}, on a transverse slice, Slice $i-1$, to its correspondence point p_i on the adjacent slice distal to it, Slice i, as V_i. Fig. 2(a) shows that when V_i points away from the centerline of the artery, the WSS value at p_i tends to be low, whereas when V_i points towards the centerline, WSS at p_i tends to be high.

To quantify this observation, we resliced the ICA (and ECA) with a 1mm interslice interval starting from the bifurcation apex. Reslicing started from the plane containing the bifurcation apex and with normal defined as the vector starting from p_{ICA} (or p_{ECA} for ECA) to the most distal point of the centerline. Ref. [18] has parameterized each branch circumferentially as shown in Fig. 1(d). Thus, each point of

the contour is equipped with a circumferential (or angular) coordinate from $-\pi$ to π. For each contour, we sampled 8 points at a regular interval at $\{\theta_i\}_{i=1}^{8}$ of the circumferential coordinate (black dots in Fig. 1(d)). The parameter *Change of Position*, ΔP, at point $x(i,j)$, the sample point on Slice i and with a circumferential coordinate of θ_j, is defined by:

$$\Delta P(x(i,j)) = [x(i,j) - x(i-1,j)] \cdot [x(i,j) - C_i] \quad (1)$$

where C_i is the intersection between the cutting plane and the centerline.

Fig. 2(b) shows the schematic of the ΔP calculation at two points. For the point on the left, V_i points towards the centreline. Thus, ΔP for this point is negative. For the point on the right, V_i points away from the centerline and ΔP is positive. We hypothesize that points with high ΔP is associated with low WSS.

We equip each sample point $x(i,j)$ with 8 parameters, which can be classified into the following four groups:

1) Change of Position: Since the ΔP in the neighbourhood of $x(i,j)$ may also have an effect of WSS, other than $\Delta P(x(i,j))$, $\Delta P(x(i-1,j))$ and $\Delta P(x(i+1,j))$ were also treated as attributes of $x(i,j)$ in the regression analysis.

2) Longitudinal and Circumferential Coordinates, L, C: The longitudinal coordinate, L, of each sample point was defined as the slice number from which the sample was taken (i.e., $L(x(i,j)) = i$). Since we observed that the WSS at a point have a correlation with its circumferential distance from the bifurcation apex, we modified the circumferential mapping described in [18] as follows: First, we found out the circumferential coordinate of the bifurcation apex and denote it as θ_b. The modified circumferential mapping, C, is the original circumferential mapping offset by θ_b (i.e., $C\,(x(i,j)) = \theta_j - \theta_b$), which reflects the circumferential distance between $x(i,j)$ and the bifurcation apex.

3) Surface Curvatures, κ_H, κ_G: Curvatures measure the "roughness" of the carotid surface. The mean (κ_H) and Gaussian curvatures (κ_G) were computed for each sample point using the technique introduced in [13].

4) Distance from Centerline, D: The size of the carotid artery may have an effect on WSS. Thus, the distance from the centerline, $D(x(i,j)) = \|x(i,j) - C_i\|$, was also used as a parameter in the regression analysis.

E. Data Analysis

The WSS at a carotid artery branch was subtracted by the mean WSS of that branch, which we denote as $DM(WSS)$. Analysis was performed on $DM(WSS)$ because the flow rate ratio between the ICA and ECA may be different for different carotid arteries. The difference in the flow rate ratio affects the mean WSS of ICA and ECA. Two linear least squares regression models were employed to quantify the relationship between $DM(WSS)$ and the 8 geometric parameters defined in Sec. II-D. In Model I, the 8 geometric parameters were used as explanatory variables. In Model II, the interaction and quadratic terms of the 8 geometric parameters were added, giving 44 explanatory variables in total. The regression models are evaluated by three parameters: root mean square error (RMSE), the adjusted R^2 and Akaike information criterion (AIC). Since comparisons were made between models with different numbers of explanatory variables and R^2 increases monotonically with the number of explanatory variables, adjusted R^2 was used to adjust for the number of explanatory variables. AIC measures the information loss when a prediction model is used to describe real data while keeping the number of explanatory variables in consideration. The preferred model is the one with minimum AIC value.

TABLE I
ADJUSTED R^2 AND RMSE FOR ICA OF EACH SUBJECT

Subject	1	2	3	4	5	6
Model I						
Adjusted R^2	0.60	0.31	0.64	0.46	0.78	0.62
RMSE	1.90	2.19	1.67	0.91	1.97	3.5
Model II						
Adjusted R^2	0.81	0.56	0.96	0.79	0.92	0.92
RMSE	1.30	1.75	0.53	0.56	1.20	1.61

TABLE II
ADJUSTED R^2 AND RMSE FOR ECA OF EACH SUBJECT

Subject	1	2	3	4	5	6
Model I						
Adjusted R^2	0.80	0.57	0.51	0.44	0.82	0.85
RMSE	1.29	1.87	2.13	1.79	0.66	1.34
Model II						
Adjusted R^2	0.91	0.85	0.80	0.73	0.91	0.93
RMSE	0.84	1.10	1.33	1.24	0.46	0.91

III. RESULTS

A. Regression For Each Individual Branch

Since each of the 6 carotid arteries has an ICA and an ECA, this study involved a total 12 carotid branches. In this section, we performed regression for the 12 branches separately. Tables I and II list the adjusted R^2 and RMSE obtained using Models I and II. Model II performs much better than Model I, giving evidence to support that $DM(WSS)$ depends on some of the second-order terms that were involved only in Model II. The adjusted R^2 for Model II ranges from 0.56 to 0.96, with 9 of the 12 branches associated with an adjusted R^2 greater than or equal to 0.8.

B. Regression For ICA and ECA With Subject Data Pooled

In this section, the data acquired for the 6 branches of ICA were pooled together in one analysis and data obtained for the 6 branches of ECA were pooled together for another analysis. For the regression performed for ICA using Model I, the adjusted R^2 was 0.29 with an AIC of 1262 and a RMSE of 2.84 Pa. When Model II was used, the adjusted R^2 improved to 0.54, the AIC reduced to 1039 and RMSE reduced to 2.21 Pa. For the regression performed for ECA using Model I, the adjusted R^2 was 0.43 with an AIC of 894 and a RMSE of 2.03 Pa. When Model II was used, the adjusted R^2 improved to 0.49, the AIC reduced to 859 and RMSE reduced to 1.92 Pa. Because of the inter-subject variability, the adjusted R^2 is lower and the RMSE higher

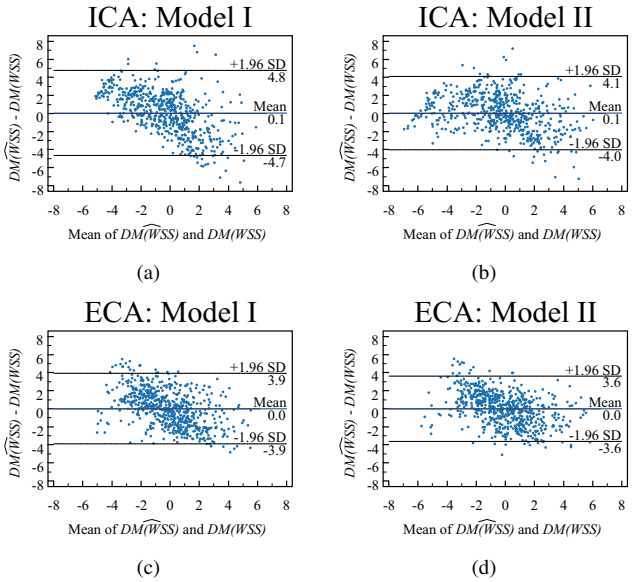

Fig. 3. Bland-Altman plots comparing $DM(WSS)$ and $\widehat{DM(WSS)}$ estimated for (a), (b) ICA and (c), (d) ECA. (a) and (c) show the Bland-Altman plots generated for estimations produced by Model I. (b) and (d) show the plots generated for estimations produced by Model II.

in the regression for the pooled data than the regressions performed for individual branches in Sec. III-A. However, when comparing the highest RMSE Model II produced (i.e., 2.21 Pa for ICA) with the precision of 0.553 Pa derived in [19] for a full CFD simulation and considering the fact that only 8 geometric parameters were involved in the regression model, Model II should be considered to perform well.

Fig. 3 shows the Bland-Altman plots [20] comparing $DM(WSS)$ and $\widehat{DM(WSS)}$ for ICA and ECA. Figs. 3(a) and 3(c) show that Model I tends to overestimate $DM(WSS)$ when WSS is lower than the average WSS of a branch (i.e., $DM(WSS) < 0$) and underestimate $DM(WSS)$ when WSS is higher than the average WSS (i.e., $DM(WSS) > 0$). Fig. 3(b) shows that this error was largely corrected for ICA by introducing Model II. However, a comparison between Figs. 3(c) and 3(d) shows that the improvement of Model II over Model I for ECA was not as apparent as for ICA. Further analysis on standardized β of first and second-order explanatory variables should be performed to acquire a better understanding on why Model II did not produce a significant improvement for ECA.

IV. Conclusion

Computing WSS using CFD is computationally intensive and time-consuming. In this paper, we defined local geometric parameters characterizing the carotid surface that can be efficiently computed and built regression models to correlate these parameters with WSS. The RMSE of our simplified model (2.21 Pa) approaches that reported for full CFD (0.553 Pa), suggesting that this rapid technique could be sufficient to highlight areas at risk due to abnormal WSS.

Notably, this study only accounted for the deviation from the mean WSS of each branch without looking into how the mean WSS would be predicted. The mean WSS is related to the average blood flow rate, which is easily obtained using Doppler ultrasound. Our future work will include correlating the average blood flow rate and mean WSS.

Acknowledgment

This work is supported by City University of Hong Kong Strategic Research Grant No. 7002762 awarded to Bernard Chiu. Gador Canton acknowledges the support by the grant T32 HL007828-13 from the National Institutes of Health.

References

[1] C. J. Schwartz and J. R. A. Mitchell, "Observations on localization of arterial plaques," *Circ. Res.*, vol. 11, pp. 63–73, 1962.
[2] M. R. Montenegro and D. A. Eggen, "Topography of atherosclerosis in the coronary arteries." *Lab Invest*, vol. 18, no. 5, pp. 586–593, May 1968.
[3] A. M. Malek, S. L. Alper, and S. Izumo, "Hemodynamic shear stress and its role in atherosclerosis." *JAMA*, vol. 282, no. 21, pp. 2035–2042, Dec 1999.
[4] A. Gnasso, C. Irace, C. Carallo, M. S. D. Franceschi, C. Motti, P. L. Mattioli, and A. Pujia, "In vivo association between low wall shear stress and plaque in subjects with asymmetrical carotid atherosclerosis." *Stroke*, vol. 28, no. 5, pp. 993–998, May 1997.
[5] I. Marshall, S. Zhao, P. Papathanasopoulou, P. Hoskins, and Y. Xu, "MRI and CFD studies of pulsatile flow in healthy and stenosed carotid bifurcation models." *J Biomech*, vol. 37, no. 5, pp. 679–687, May 2004.
[6] S. Z. Zhao, P. Papathanasopoulou, Q. Long, I. Marshall, and X. Y. Xu, "Comparative study of magnetic resonance imaging and image-based computational fluid dynamics for quantification of pulsatile flow in a carotid bifurcation phantom." *Ann Biomed Eng*, vol. 31, no. 8, pp. 962–971, Sep 2003.
[7] D. A. Steinman, "Image-based computational fluid dynamics modeling in realistic arterial geometries," *Ann Biomed Eng*, vol. 30, no. 4, pp. 483–497, Apr 2002.
[8] S.-W. Lee, L. Antiga, and D. A. Steinman, "Correlations among indicators of disturbed flow at the normal carotid bifurcation." *J Biomech Eng*, vol. 131, no. 6, p. 061013, Jun 2009.
[9] G. Canton, B. Chiu, C. Yuan, and W. Kerwin, "Correlation of hemodynamic forces and atherosclerotic plaque components," *Proc. SPIE*, vol. 7625, p. 76250G, 2008.
[10] M. Markl, F. Wegent, T. Zech, S. Bauer, C. Strecker, M. Schumacher, C. Weiller, J. Hennig, and A. Harloff, "In vivo wall shear stress distribution in the carotid artery: effect of bifurcation geometry, internal carotid artery stenosis, and recanalization therapy." *Circ Cardiovasc Imaging*, vol. 3, no. 6, pp. 647–655, Nov 2010.
[11] S.-W. Lee, L. Antiga, J. D. Spence, and D. A. Steinman, "Geometry of the carotid bifurcation predicts its exposure to disturbed flow." *Stroke*, vol. 39, no. 8, pp. 2341–2347, Aug 2008.
[12] J. B. Thomas, L. Antiga, S. L. Che, J. S. Milner, D. A. H. Steinman, J. D. Spence, B. K. Rutt, and D. A. Steinman, "Variation in the carotid bifurcation geometry of young versus older adults: implications for geometric risk of atherosclerosis." *Stroke*, vol. 36, no. 11, pp. 2450–2456, Nov 2005.
[13] B. Chiu, V. Beletsky, J. D. Spence, G. Parraga, and A. Fenster, "Analysis of carotid lumen surface morphology using three-dimensional ultrasound imaging," *Phys. Med. Biol.*, vol. 54, no. 5, pp. 1149–1167, Mar 7 2009.
[14] W. Kerwin, D. Xu, F. Liu, T. Saam, H. Underhill, N. Takaya, B. Chu, T. Hatsukami, and C. Yuan, "Magnetic resonance imaging of carotid atherosclerosis: plaque analysis," *Top Magn Reson Imaging*, vol. 18, no. 5, pp. 371–378, Oct 2007.
[15] P. Persson and G. Strang, "A simple mesh generator in MATLAB," *SIAM review*, vol. 46, no. 2, pp. 329–345, 2004.
[16] W. Kerwin and C. Yuan, "Three dimensional surface models of carotid atherosclerosis," in *Signal and Image Processing*, N. Younan, Ed. ACTA Press, 2002, pp. 589 – 594.
[17] W. Lorensen and H. Cline, "Marching cubes: A high resolution 3D surface construction algorithm," *ACM Siggraph Computer Graphics*, vol. 21, no. 4, pp. 163–169, 1987.
[18] L. Antiga and D. A. Steinman, "Robust and objective decomposition and mapping of bifurcating vessels," *IEEE Trans. Med. Imaging*, vol. 23, no. 6, pp. 704–713, Jun 2004.
[19] F. P. Glor, Q. Long, A. D. Hughes, A. D. Augst, B. Ariff, S. A. M. Thom, P. R. Verdonck, and X. Y. Xu, "Reproducibility study of magnetic resonance image-based computational fluid dynamics prediction of carotid bifurcation flow." *Ann Biomed Eng*, vol. 31, no. 2, pp. 142–151, Feb 2003.
[20] J. M. Bland and D. G. Altman, "Measuring agreement in method comparison studies." *Stat Methods Med Res*, vol. 8, no. 2, pp. 135–160, Jun 1999.